

# Interplay of superexchange and vibronic effects in the hidden order of $\text{Ba}_2\text{MgReO}_6$ unravelled from first principles

Dario Fiore Mosca,<sup>1,2</sup> Cesare Franchini,<sup>3,4</sup> and Leonid V. Pourovskii<sup>1,2</sup>

<sup>1</sup>*CPHT, CNRS, École polytechnique, Institut Polytechnique de Paris, 91120 Palaiseau, France*

<sup>2</sup>*Collège de France, Université PSL, 11 place Marcelin Berthelot, 75005 Paris, France*

<sup>3</sup>*University of Vienna, Faculty of Physics and Center for Computational Materials Science, Vienna, Austria*

<sup>4</sup>*Department of Physics and Astronomy "Augusto Righi",*

*Alma Mater Studiorum - Università di Bologna, Bologna, 40127 Italy*

The origin of the "hidden" quadrupolar and unconventional magnetic low-temperature orders observed in the spin-orbit double perovskite  $\text{Ba}_2\text{MgReO}_6$  defies explanation through standard experimental and theoretical techniques. Here we address this problem by deriving and solving an ab initio low-temperature effective Hamiltonian including inter-site electronic exchange and vibronic (electron-lattice) couplings between  $J_{\text{eff}} = 3/2$  Jahn-Teller-active Rhenium states. Our findings disclose the nature of these elusive states, attributing it to intertwined exchange and electron-lattice couplings, thus diverging from the conventional dichotomy of purely electronic or lattice driving mechanisms. Our results indicate the resilience of the quadrupolar hidden order under pressure, yet its rapid suppression under uniaxial strain suggests that external or lattice-induced distortions play a pivotal role in determining the relative stability of competing phases in  $\text{Ba}_2\text{MgReO}_6$  and similar  $d^1$  double perovskites.

**Introduction.** Correlated insulators with strong spin-orbit (SO) have recently emerged as a rich playground for unconventional low-temperature orders and exotic states of matter [1–4]. In particular, heavy transition-metal (TM) compounds have been found to exhibit a wide range of exotic phases, including the elusive Kitaev spin liquid in SO  $d^5$  Mott insulators [5, 6] and complex high-rank magnetic and charge multipolar orders in  $d^1$  and  $d^2$  SO double perovskites (DP) and halides [7–12]. Revealing and interpreting the origin of these exotic phases poses a formidable challenge, given their hidden nature that eludes conventional experimental probes [13].

Initially, theoretical investigations primarily centered on electronic exchange and electrostatic interactions as the fundamental driving forces behind the unconventional orders observed in  $5d^1$  and  $5d^2$  SO DP [14–16]. While the spin-orbit-entangled ground states in a cubic crystal field have been recognized as Jahn-Teller (JT) active [2], a possibly crucial role of electron-lattice (EL) interactions in these compounds has only recently gained recognition [17–20]. The interplay between EL and purely electronic couplings adds layers of complexity, as their relative strength and roles in the unconventional orders remain poorly understood. Gaining insight into the correlation between JT effects and electronic exchange could provide access to physical regimes that are presently inaccessible.

A prototypical example is the Mott insulating double perovskite  $\text{Ba}_2\text{MgReO}_6$  (BMRO here after). Experimental high-resolution x-ray diffraction and resonant elastic x-ray scattering (REXS) resolve two phase transitions occurring upon lowering the temperature [2, 9, 20, 21]. The first transition at  $T_q \approx 33$  K is concomitant with a lattice distortion reducing the symmetry of the  $Fm\bar{3}m$  parent cubic structure. It is followed by the emergence of

a canted antiferromagnetic (cAFM) phase at  $T_m \approx 18$  K with net magnetization along [110] axis. Under applied pressure, the high- $T$  phase is suppressed and, simultaneously, the cAFM order transforms to a pure AFM one [22]. Among various  $d^1$  DP  $\text{Ba}_2M\text{ReO}_6$  compounds, two phase transitions are observed for  $M=\text{Mg}$ ,  $\text{Zn}$ , and  $\text{Cd}$  [9, 23, 24], but only a single AFM phase is found for  $M=\text{Ca}$  [25, 26].

Hirai and coworkers [9] assigned the transition at  $T_q$  to the onset of a purely quadrupolar phase consisting of  $x^2 - y^2$  anti-ferroic ( $\text{AF}x^2 - y^2$ ) and  $z^2$  ferroic components ( $\text{F}z^2$ ), as inferred from the observed reduction of the lattice symmetry to tetragonal  $P42/mnm$ . A similar picture – of a high- $T$  quadrupolar  $\text{AF}x^2 - y^2$  phase followed by the onset of a low- $T$  cAFM order – was previously shown to emerge from intersite exchange (IE) models supplemented by a sizeable electrostatic quadrupolar interaction [14, 16]. Inspired by these theories, Refs. [9, 22, 23] attempted to construct a generic phase diagram for  $d^1$  DP linking the disappearance of quadrupolar  $\text{AF}x^2 - y^2$  and cAFM phases in BMRO under pressure and their absence in  $\text{Ba}_2\text{CaReO}_6$  to the volume dependence of superexchange and electrostatic quadrupolar couplings.

Iwahara and colleagues [18] suggested an alternative EL-dominated model for  $d^1$  DP and halides that is based on strong JT coupling between  $e_g$  quadrupoles combined with a system independent IE term. They successfully reproduced both the composite quadrupolar order and cAFM phases, although for a specific set of parameters.

The different highlighted schemes thus reduce the problem to the contradictory purely electronic [14, 16, 27] or EL-dominated limits [18]. First principles calculations for BMRO and analogous compounds suggest that the observed ground-state magnetic order cannot be ex-

plained without invoking JT distortions [19, 28]. Soh et al. [20] estimated the energy of cooperative JT distortions in DFT finding it to totally dominate over electronic exchange and to force the  $AFx^2 - y^2$  order. Importantly, in all these ab initio studies JT dynamics has not been included.

The available literature thus hints at a delicate balance between EL and IE mechanisms in BMRO that necessitates their treatment on the equal footing, validated by fully ab initio computations of materials-specific interaction parameters.

In this Letter, we propose an advanced ab initio framework for deriving a low-energy many-body effective Hamiltonian (MBEH) of SO Mott insulators that fully includes both IE and EL interactions. Deriving such a MBEH for BMRO and solving it by a consistent single-site mean-field theory we reproduce both the  $AFx^2 - y^2$  and cAFM orders. We find that BMRO is in a weak JT coupling limit and that neither IE nor EL terms alone can account for the observed quadrupolar order. A faithful representation of the physics of BMRO becomes possible only by incorporating both interactions. We also find upon varying volume that EL and IE terms largely compensate each other. The overall picture - of the high- $T$   $AFx^2 - y^2$  and low- $T$  cAFM orders - remains remarkably unchanged over quite a broad range. In contrast, small strains are predicted to rapidly suppress the quadrupolar order and induce a collinear AFM phase, thus explaining the findings of Arima and coworkers by non-hydrostatic pressure conditions [22].

*Effective Hamiltonian.* In the  $5d^1$  cubic DP, the ground state multiplet is determined by the combined action of crystal field and SO coupling. The former, splitting the 5d orbitals in  $e_g$  and  $t_{2g}$  states, produces an effective orbital momentum  $l = 1$  which couples to the spin  $S = 1/2$ , promoting the  $J_{\text{eff}} = 3/2$  SO-coupled ground state wavefunctions. The full microscopic MBEH contains three components, an electronic part, the local JT activity and the intersite elastic couplings (EC):

$$H_{\text{eff}} = H_{\text{IEI}} + H_{\text{JT}} + H_{\text{EC}}. \quad (1)$$

The electronic-mediated IE interactions (IEI) between the multipolar moments with defined total angular momentum  $J = 3/2$  are described by the effective Hamiltonian

$$H_{\text{IEI}} = \sum_{\langle ij \rangle} \sum_{K, K', Q, Q'} V_{KK'}^{QQ'}(ij) O_K^Q(i) O_{K'}^{Q'}(j) \quad (2)$$

where the first summation  $(ij)$  runs over the Re-Re bonds, the second one over the multipolar momenta of the ranks  $K, K'=1, 2, 3$  and projections  $Q, Q' = -K \dots K$ ,  $O_K^Q(i)$  is the normalized multipolar operator [3] acting on the site  $i$ ,  $V_{KK'}^{QQ'}(ij)$  represents the corresponding IEI.

The  $J_{\text{eff}} = 3/2$  multiplet is JT active with the corresponding quadrupole moments coupled to the irreducible

distortions  $\{T_{2g}, E_g\}$  of the  $\text{ReO}_6$  octahedron via

$$H_{\text{JT}} = \sum_{i, \Gamma} \sum_{Q \in \Gamma} \frac{p_Q^2(i)}{2M_\Gamma} + \Phi_\Gamma \frac{q_{\Gamma Q}^2(i)}{2} - g_\Gamma O_2^Q(i) q_{\Gamma Q}(i) \quad (3)$$

where  $\Gamma \in \{T_{2g}, E_g\}$ , while  $Q$  runs over the distortion modes belonging to  $\Gamma$ . Here  $\Phi_\Gamma$  is the diagonal term of the irreducible force-constant matrix,  $q_{\Gamma Q}(i)$  is the distortion associated with the irreducible mode,  $p_Q(i)$  and  $M_\Gamma$  are the corresponding momentum and reduced mass, respectively,  $g_\Gamma$  is the JT coupling constant that couples the distortion  $q_{\Gamma Q}(i)$  to the electronic quadrupole operator  $O_2^Q(i)$ .

Lastly, JT distortions on neighboring octahedral centers interact with each other through elastic couplings

$$H_{\text{EC}} = \sum_{\langle ij \rangle} \sum_{\Gamma \Gamma'} \sum_{Q \in \Gamma} \sum_{Q' \in \Gamma'} \Phi_{\Gamma \Gamma'}^{QQ'}(ij) q_{\Gamma Q}(i) q_{\Gamma' Q'}(j), \quad (4)$$

where the summation  $(ij)$  goes over Re pairs, and  $\Phi_{\Gamma \Gamma'}^{QQ'}$  is the irreducible force constant matrix coupling distortions of the oxygen cage at the sites  $i$  and  $j$ .

*Methods.* We determine all coupling constants in Eq. 1 from first principles. The IEI are computed by the force-theorem approach of Ref. [29] from the converged paramagnetic electronic structure of cubic BMRO obtained by charge self-consistent density-functional theory (DFT) [30] + dynamical mean-field theory [31–34] in the quasi-atomic Hubbard-I (HI) [35] approximation, see Supplemental Material (SM) [36] for further details. Our DFT+HI calculations correctly reproduce the  $\text{Re}^{6+}$  ground state multiplet  $J = 3/2$ , the corresponding SO splitting between  $J = 3/2$  and  $J = 1/2$  states ( $\approx 0.44$  eV) and the crystal field splitting ( $\approx 4.5$  eV). The JT coupling constants  $g_\Gamma$  are also obtained with DFT+HI by calculating a set of distorted BMRO structures for a chosen mode that is consistent with the order parameter and induces local octahedral distortions  $Q \in \Gamma$ . We then extract  $g_\Gamma$  by fitting the calculated  $J = 3/2$  level splitting as a function of the mode amplitude (see the SM [36]).

Both on-site elastic constant in  $H_{\text{JT}}$  and inter-site couplings in  $H_{\text{EC}}$  have been obtained from the force constant matrix of a density functional perturbation theory calculation [37, 38] projected onto the irreducible JT modes of the ligand ions via

$$\Phi_{\Gamma \Gamma'}^{QQ'}(ij) = \sum_{\alpha, \beta} (C_{\Gamma Q}^\alpha)^\dagger \Phi_{\alpha \beta}(ij) (C_{\Gamma' Q'}^\beta), \quad (5)$$

where  $\Phi_{\alpha \beta}(ij)$  is the force constant matrix in the Cartesian coordinate reference frame of components  $(\alpha, \beta)$  for atomic sites  $(i, j)$ . The projected force constants are obtained through change of coordinate on the ligand ions  $r_{\Gamma Q} = \sum_\alpha C_{\Gamma Q}^\alpha r_\alpha$ .

We note that our calculations predict only the nearest-neighbor IEI terms in Eq. 2 to be substantial in BMRO.

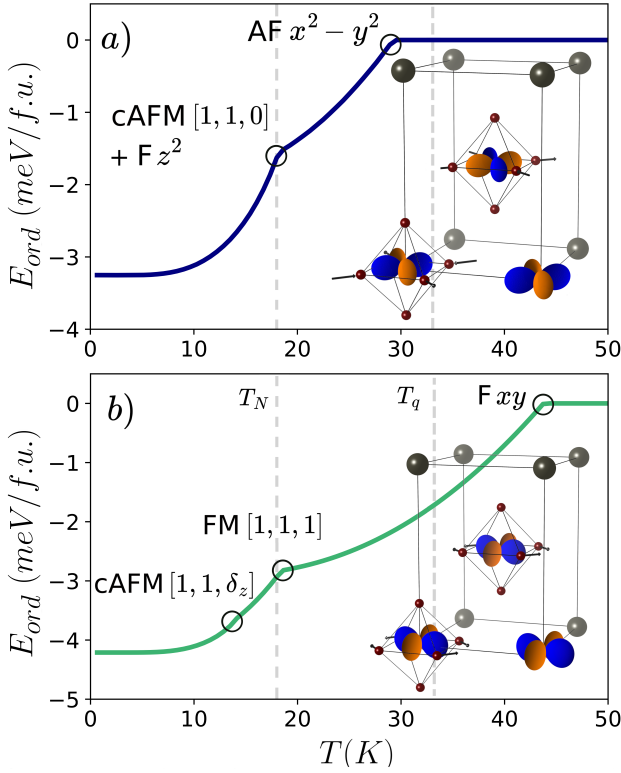


FIG. 1: Mean-field ordering energy vs. temperature calculated from the Hamiltonian eq. 1 with (a) all interactions included and (b) from  $H_{IEI}$  only. The insets depict the AF  $x^2 - y^2$  (a) Fxy (b) ordered phases respectively, with associated JT distortions. The dashed lines mark the magnetic and quadrupolar measured temperatures [9].

The longer-range IEI terms are deemed negligible, aligning with expectations for superexchange and consistent with our prior findings. [12, 19, 39]. The inclusion of next-nearest neighbors EC in Eq. 4 is necessary for reproducing the phonon spectra at the commensurate points with good accuracy (see SM [36]).

**JT regime.** Our calculations predict that  $E_g$  modes are almost 3 times more strongly JT-coupled than the  $T_{2g}$  ones,  $g_{E_g} = 1.53$  eV/Å and  $g_{T_{2g}} = 0.58$  eV/Å. The resulting JT stabilization energy (i. e. the depth of the JT potential well)  $E_{JT} = g_{E_g}/8\Phi_{E_g} \approx 14$  meV, well below the oscillatory frequency of the  $E_g$  modes  $\hbar\omega_{E_g} \approx 75$  meV, places BMRO in the weak coupling regime, in contrast to previous assumptions suggesting a strong coupling regime [18]. Our numerical tests on the single-site JT problem indeed show that the vibronic basis cut to one phonon – corresponding to a weak-coupling treatment of the JT problem [40] – already provides reasonably high accuracy for the ground-state energy (see SM [36]).

**Ordered phases.** As a next step we solve the Eq. 1 within a single-site mean field (MF) [41] by decoupling

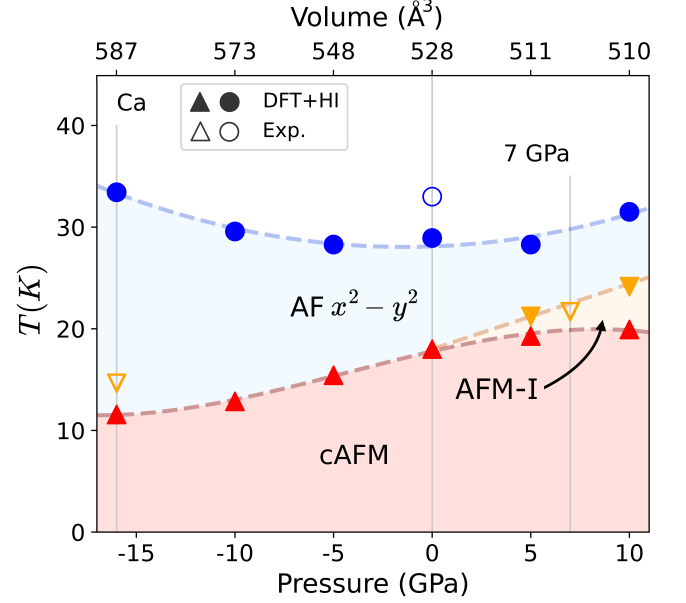


FIG. 2: Mean-field phase diagram of BMRO at different pressures. The full circles and triangles represent the computed points, while the empty are experimental results. The 7 GPa exp. is from Ref. [22], the -16 GPa point corresponds to the Ca compound of Ref. [25]. Upright and inverted triangles mark the cAFM [110], AFM-I transition temperatures, while circles mark the AF  $x^2 - y^2$  phase.

both the IEI (Eq. 2) and EC (Eq. 4) terms and solving the single-site JT problem in mean-field in the weak-coupling limit. We find that BMRO undergoes two second-order phase transitions at temperatures  $T_q \approx 45$  K and  $T_m \approx 28$  K. The calculated values are systematically overestimated by  $\sim 40\%$  as a consequence of the MF + HI approximation [12, 42, 43]. We have thus reduced the transition temperatures in our phase diagrams (Figures 1 and 2) by this constant factor. Our findings align well with experimental observations, showing a charge quadrupolar AF  $x^2 - y^2$  order with wave vector  $\mathbf{k} = [0, 0, 1]$  below  $T_q$ , and cAFM configuration with the net moment along [110] below  $T_m$ . Our data does not reveal any ferroic  $Fz^2$  in the quadrupolar region though it manifests below  $T_m$ . Its occurrence above  $T_m$  in experiment might be due to high-order elastic couplings that are not accounted for in our model. It is worth noting that the measured magnitude of the  $z^2$  distortion at low temperatures is twice as large as the corresponding value at 25 K and does not appear to behave as a primary order parameter [9].

Simultaneously with  $Fz^2$ , the  $t_{2g}$   $xy$  charge quadrupole also orders ferroically below  $T_m$ . The corresponding amplitude of the Fxy distortion mode is more than an order of magnitude smaller than that of the AF  $x^2 - y^2$  mode. In contrast, the ratio between  $x^2 - y^2$  and  $z^2$  distortion modes is  $\sim 4.6$ , as compared to exper-

imental ratio of  $\sim 4.5$  [9], though the predicted  $x^2 - y^2$  distortion magnitude (0.021 Å) is underestimated.

In order to investigate competing orders and comprehend the influence of EL interactions on the stability of the observed  $\text{AF}x^2 - y^2$  and cAFM phases, we conducted calculations with the JT and EC terms set to zero. We obtained (Fig. 1b) (i) ferro-quadrupolar  $xy$  (or equivalently  $xz/yz$ ) phase ( $\text{F}xy$ ) at temperature  $T_q \approx 68$  K, followed by (ii) collinear ferromagnetic with [111] easy axis at  $T_{FM} \approx 28$  K and (iii) cAFM with easy axis along  $[1, 1, \delta_z]$  at  $T_{m'} \approx 22$  K, with  $\delta_z = 0.67$  as  $T \rightarrow 0$ . This demonstrates that vibronic interactions play a crucial role in determining both charge and magnetic order, particularly in establishing the observed  $\text{AF}x^2 - y^2$  state. The quadrupolar IEI alone, in the absence of local and non-local lattice interactions, favor ferro-quadrupolar  $\text{F}xy$ , as follows from the IEI structure; in fact the  $t_{2g}$  IEI, which were overlooked in the electronic models of Refs. [14, 16, 27], exhibit a ferroic nature and are nearly equal in magnitude to the antiferroic  $e_g$ . Importantly, the ferroic order is not frustrated by the Re sublattice geometry.

To verify the essential role played by EC in stabilizing  $\text{AF}x^2 - y^2$  phase we compared three different scenarios: (i) Considering only IEI, the total energy difference  $\Delta E$  between  $\text{F}xy$  and  $\text{AF}x^2 - y^2$  is -1.46 meV. (ii) Introducing the local JT coupling term reinforces the stability of  $\text{F}xy$ , resulting in  $\Delta E = -2.11$  meV. (iii) However, upon adding non-local EC, the energy balance is reversed, favoring the AF order with  $\Delta E = 0.71$  meV. Moreover, we also carried out calculations with only EL (the JT and EC terms) included. This results in a pure  $\text{F}z^2$  order (that is actually experimentally found in related  $d^1$  halides [10]) with  $T_q \approx 20$  K. Hence, neither the EL term alone can account for the correct QP order in BMRO.

*Effect of hydrostatic pressure.* Arima and coworkers recently observed that pressures higher than  $\approx 7$  GPa suppress the  $\text{AF}x^2 - y^2$  phase in BMRO and induce a cAFM to collinear AFM transition [22]. To understand the role of pressure on BMRO, we computed the IEI, JT and EC Hamiltonians as a function of pressure  $P$  between -16 GPa (corresponding to the volume of  $\text{Ba}_2\text{CaReO}_6$ ) and 10 GPa. Our results (Figure 2) highlight the persistence of both  $\text{AF}x^2 - y^2$  and cAFM phase at all pressures. For positive values, the  $\text{AF}x^2 - y^2$  approaches the magnetic ordering, without any crossing and a small AFM region appears above the cAFM one. This AFM phase has a  $2\mathbf{k}$  structure with magnetic moments lying in the  $xz$  plane (AFM-I). For negative pressures the  $T_q$  increases, while the  $T_m$  decreases. To decipher the peculiar behavior of quadrupolar and magnetic transition temperatures, we have performed a *gedankenexperiment* consisting in either keeping IEI fixed at the 0 GPa values while tuning the EL interactions or vice versa. Our results (Fig. 3) show that the temperature behavior of  $T_m$  is accurately captured using only IEI. However, re-

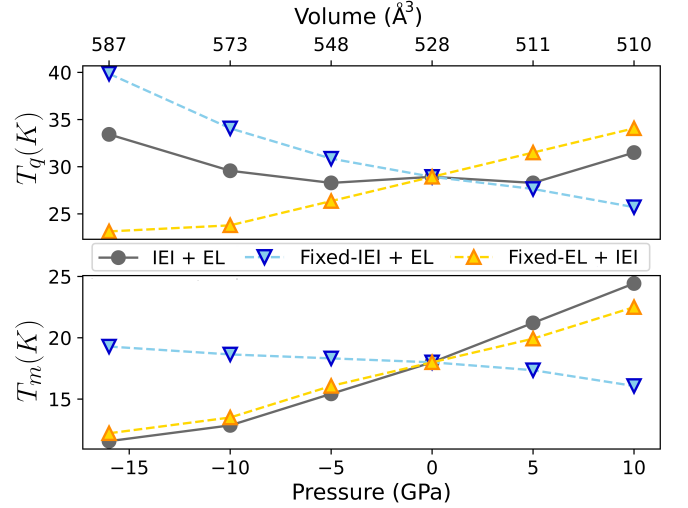


FIG. 3: Mean-field transition temperatures dependence of  $T_q$  (top) and  $T_m$  (bottom), as a function of pressure for the full Hamiltonian of eq. 1 (filled circles). Together are plotted the solutions obtained with IEI fixed to 0 GPa, while varying EL interactions (inverted triangles) or with fixed EL, while varying IEI interactions (upright triangles).

garding the quadrupolar phase, we note that while IEI alone would lead to a rise in the transition temperature as  $P$  increases, the EL interactions counter act this effect by lowering it. In the end, it is the interplay between these two tendencies that shapes the observed temperature curve.

Therefore, our calculations reveal, in contrast to previous assumptions [9, 22, 23], that volume change does not qualitatively affect the phase stability in  $d^1$  Re DP. Neither for the large-volume limit ( $P = -16$  GPa, corresponding to  $\text{Ba}_2\text{CaReO}_6$ ) nor under the highest pressure in Arima measurements (10 GPa) we do find the experimentally observed collapse of the quadrupolar order and onset of the collinear AFM. This apparent contradiction can be understood by considering non-isotropic pressure as elaborated in the following.

*Effect of strain.* Glycerol pressure-transmitting medium used in Arima's experiment [22] does not ensure perfect hydrostaticity above 5 GPa, potentially leading to uniaxial stresses. To explore the impact of uniaxial strains in compressed BMRO, we introduced an on-site term to our effective Hamiltonian (Eq. 1). This term is given by  $H_{\text{strain}} = K\delta O_2^0(i)$ , with  $\delta = c/a - 1$ , where  $K = -3.0$  eV was estimated from DFT+HI calculations for tetragonally distorted BMRO akin to the JT coupling.

For  $P = 10$  GPa and the range  $\delta \in [-2.5 \cdot 10^{-3}, 2.5 \cdot 10^{-3}]$ , which corresponds to a tetragonal distortion of the unit cell of maximum  $\pm 0.02$  Å, we obtain the phase diagram shown in Figure 4. It features four regions:  $\text{AF}x^2 - y^2$ , cAFM [110], AFM-I and AFM-II, the



last being a collinear AFM structure with wave vector  $\mathbf{k} = [0, 0, 1]$ . While the cAFM and AFM-I MF solutions form asymmetric regions, the  $\text{AF}x^2 - y^2$  phase is suppressed on the both sides for  $|\delta| > 2 \cdot 10^{-3}$  in favour of the collinear AFM-I due to easy-plane(axis) single-ion anisotropy induced by tetragonal compression (elongation) by  $H_{\text{strain}}$ . Our calculations thus predict that even small deviations from hydrostaticity will lead to the suppression of the quadrupolar order and appearance of a collinear AFM reported in Ref. [22].

**Conclusions.** We have derived an ab initio many-body effective Hamiltonian for BMRO, incorporating both electronic and vibronic interactions. Our evaluation of the ordered phases for BMRO under ambient conditions, as well as hydrostatic and non-hydrostatic pressure, reveals that the experimentally observed  $\text{AF}x^2 - y^2$  quadrupolar order and non-collinear canted AFM phases are stabilized by a subtle interplay of intertwined exchange and electron-lattice interactions. We find that the volume effect on phase stability is qualitatively insignificant. In contrast, even minute strains rapidly suppress the quadrupolar order and promote the stabilization of a collinear AFM state. These results enhance our understanding of the entire  $d^1$  double perovskite series. Furthermore, our data suggest that small purely lattice distortions, observed, for instance, in both  $\text{Ba}_2\text{CaReO}_6$  [25] and  $\text{Ba}_2\text{CdReO}_6$  [23], rather than volume, can be the key parameter controlling their low-temperature order. The broad applicability of the proposed ab initio approach shows potential for use in other Mott insulators char-

acterized by spin-orbit entangled and Jahn-Teller-active ground state multiplets in the bulk as well as in the 2D limit. This method holds promise for uncovering novel quantum states of matter and furnishing essential theoretical insights to interpret the underlying driving mechanisms.

We acknowledge useful discussions with N. Iwahara, M. Merkel and J.-R. Son. Support by the the Austrian Science Fund (FWF) grant J4698 is gratefully acknowledged. C.F. acknowledge financial support by the European Union – Next Generation EU - “PNRR - M4C2, investimento 1.1 - Fondo PRIN 2022” - “Superlattices of relativistic oxides” (ID 2022L28H97, CUP D53D23002260006). D. F. M. thanks C. Verdi and L. Ranalli for the useful discussions and acknowledges the computational facilities of the Vienna Scientific Cluster (VSC). L. V. P. is thankful to the CPHT computer team for support.

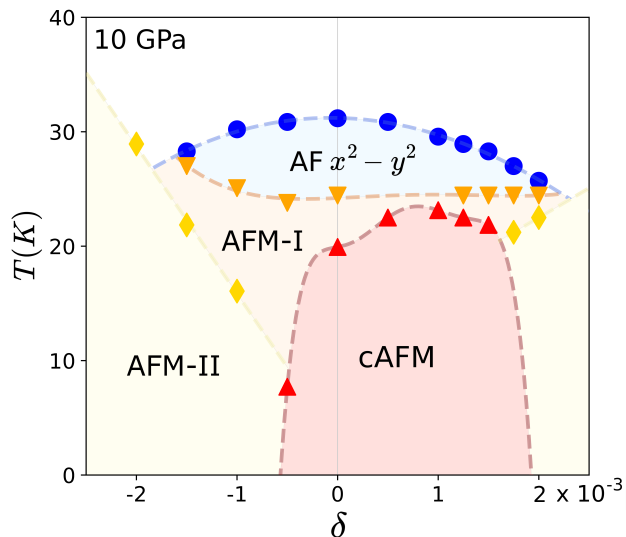


FIG. 4: Mean-field phase diagram showing the evolution of BMRO at 10 GPa under uniaxial strain. Four phases can be distinguished: (i)  $\text{AF}x^2 - y^2$  as circles, (ii) cAFM as upright triangles (iii) AFM-I as inverted triangles and (iv) AFM-II as diamonds. The curves are obtained from polynomial fits of the data points.

- 
- [1] W. Witczak-Krempa, G. Chen, Y. B. Kim, and L. Balents, Annual Review of Condensed Matter Physics **5**, 57 (2014).
  - [2] T. Takayama, J. Chaloupka, A. Smerald, G. Khaliullin, and H. Takagi, Journal of the Physical Society of Japan **90**, 062001 (2021).
  - [3] P. Santini, S. Carretta, G. Amoretti, R. Caciuffo, N. Magnani, and G. H. Lander, Rev. Mod. Phys. **81**, 807 (2009).
  - [4] Y. Kuramoto, H. Kusunose, and A. Kiss, Journal of the Physical Society of Japan **78**, 072001 (2009).
  - [5] H. Takagi, T. Takayama, G. Jackeli, G. Khaliullin, and S. E. Nagler, Nature Reviews Physics **1**, 264 (2019).
  - [6] G. Jackeli and G. Khaliullin, Phys. Rev. Lett. **102**, 017205 (2009).
  - [7] D. D. Maharaj, G. Sala, M. B. Stone, E. Kermarrec, C. Ritter, F. Fauth, C. A. Marjerrison, J. E. Greedan, A. Paramekanti, and B. D. Gaulin, Phys. Rev. Lett. **124**, 087206 (2020).
  - [8] L. Lu, M. Song, W. Liu, A. P. Reyes, P. Kuhns, H. O. Lee, I. R. Fisher, and V. F. Mitrović, Nature Communications **8**, 14407 (2017).
  - [9] D. Hirai, H. Sagayama, S. Gao, H. Ohsumi, G. Chen, T.-h. Arima, and Z. Hiroi, Phys. Rev. Res. **2**, 022063 (2020).
  - [10] H. Ishikawa, T. Takayama, R. K. Kremer, J. Nuss, R. Dinnebier, K. Kitagawa, K. Ishii, and H. Takagi, Phys. Rev. B **100**, 045142 (2019).
  - [11] A. Paramekanti, D. D. Maharaj, and B. D. Gaulin, Phys. Rev. B **101**, 054439 (2020).
  - [12] L. V. Pourovskii, D. F. Mosca, and C. Franchini, Phys. Rev. Lett. **127**, 237201 (2021).
  - [13] J. A. Mydosh and P. M. Oppeneer, Rev. Mod. Phys. **83**, 1301 (2011).
  - [14] G. Chen, R. Pereira, and L. Balents, Phys. Rev. B **82**, 174440 (2010).
  - [15] G. Chen and L. Balents, Phys. Rev. B **84**, 094420 (2011).
  - [16] C. Svoboda, W. Zhang, M. Randeria, and N. Trivedi,

- Phys. Rev. B **104**, 024437 (2021).
- [17] N. Iwahara, V. Vieru, and L. F. Chibotaru, Phys. Rev. B **98**, 075138 (2018).
  - [18] N. Iwahara and L. F. Chibotaru, Phys. Rev. B **107**, L220404 (2023).
  - [19] D. Fiore Mosca, L. V. Pourovskii, B. H. Kim, P. Liu, S. Sanna, F. Boscherini, S. Khmelevskyi, and C. Franchini, Phys. Rev. B **103**, 104401 (2021).
  - [20] J.-R. Soh, M. E. Merkel, L. Pourovskii, I. Živković, O. Malanyuk, J. Pásztorová, S. Francoual, D. Hirai, A. Urru, D. Tolj, D. Fiore-Mosca, O. Yazyev, N. A. Spaldin, C. Ederer, and H. M. Rønnow, “Spectroscopic signatures and origin of a hidden order in  $\text{Ba}_2\text{MgReO}_6$ ,” (2023), arXiv:2312.01767 [cond-mat.str-el].
  - [21] C. A. Marjerrison, C. M. Thompson, G. Sala, D. D. Maharaj, E. Kermarrec, Y. Cai, A. M. Hallas, M. N. Wilson, T. J. S. Munsie, G. E. Granroth, R. Flacau, J. E. Greedan, B. D. Gaulin, and G. M. Luke, Inorganic Chemistry **55**, 10701 (2016).
  - [22] H. Arima, Y. Oshita, D. Hirai, Z. Hiroi, and K. Matsumabayashi, Journal of the Physical Society of Japan **91**, 013702 (2022).
  - [23] D. Hirai and Z. Hiroi, Journal of Physics: Condensed Matter **33**, 135603 (2021).
  - [24] V. da Cruz Pinha Barbosa, J. Xiong, P. M. Tran, M. A. McGuire, J. Yan, M. T. Warren, R. V. Aguilar, W. Zhang, M. Randeria, N. Trivedi, D. Haskel, and P. M. Woodward, Chemistry of Materials **34**, 1098 (2022).
  - [25] K. Yamamura, M. Wakeshima, and Y. Hinatsu, Journal of Solid State Chemistry **179**, 605 (2006).
  - [26] H. Ishikawa, D. Hirai, A. Ikeda, M. Gen, T. Yajima, A. Matsuo, Y. H. Matsuda, Z. Hiroi, and K. Kindo, Phys. Rev. B **104**, 174422 (2021).
  - [27] H. Kubo, T. Ishitobi, and K. Hattori, Phys. Rev. B **107**, 235134 (2023).
  - [28] A. Mansouri Tehrani and N. A. Spaldin, Phys. Rev. Mater. **5**, 104410 (2021).
  - [29] L. V. Pourovskii, Phys. Rev. B **94**, 115117 (2016).
  - [30] P. Blaha, K. Schwarz, G. Madsen, D. Kvasnicka, J. Luitz, R. Laskowski, F. Tran, and L. D. Marks, *WIEN2k, An augmented Plane Wave + Local Orbitals Program for Calculating Crystal Properties* (Karlheinz Schwarz, Techn. Universität Wien, Austria, ISBN 3-9501031-1-2, 2018).
  - [31] A. Georges, G. Kotliar, W. Krauth, and M. J. Rozenberg, Rev. Mod. Phys. **68**, 13 (1996).
  - [32] V. I. Anisimov, A. I. Poteryaev, M. A. Korotin, A. O. Anokhin, and G. Kotliar, Journal of Physics: Condensed Matter **9**, 7359 (1997).
  - [33] A. I. Lichtenstein and M. I. Katsnelson, Phys. Rev. B **57**, 6884 (1998).
  - [34] M. Aichhorn, L. Pourovskii, P. Seth, V. Vildosola, M. Zingl, O. E. Peil, X. Deng, J. Mravlje, G. J. Kraberger, C. Martins, *et al.*, Computer Physics Communications **204**, 200 (2016).
  - [35] J. Hubbard, Proc. Roy. Soc. (London) **A 276**, 238 (1963).
  - [36] Supplementary Material.
  - [37] M. Gajdoš, K. Hummer, G. Kresse, J. Furthmüller, and F. Bechstedt, Phys. Rev. B **73**, 045112 (2006).
  - [38] P. Giannozzi, S. de Gironcoli, P. Pavone, and S. Baroni, Phys. Rev. B **43**, 7231 (1991).
  - [39] L. V. Pourovskii, Phys. Rev. B **108**, 054436 (2023).
  - [40] I. B. Bersuker and V. Z. Polinger, *Vibronic Interactions in Molecules and Crystals* (Springer Berlin Heidelberg, 1989).
  - [41] M. Rotter, Journal of Magnetism and Magnetic Materials **272-276, Supplement**, E481 (2004).
  - [42] A. Horvat, L. Pourovskii, M. Aichhorn, and J. Mravlje, Phys. Rev. B **95**, 205115 (2017).
  - [43] L. V. Pourovskii and S. Khmelevskyi, Phys. Rev. B **99**, 094439 (2019).

# Supplementary material for 'Interplay of superexchange and vibronic effects in the hidden order of Ba<sub>2</sub>MgReO<sub>6</sub> unravelled from first principles'

Dario Fiore Mosca,<sup>1,2</sup> Cesare Franchini,<sup>3,4</sup> and Leonid V. Pourovskii<sup>1,2</sup>

<sup>1</sup>*CPHT, CNRS, École polytechnique, Institut Polytechnique de Paris, 91120 Palaiseau, France*

<sup>2</sup>*Collège de France, Université PSL, 11 place Marcelin Berthelot, 75005 Paris, France*

<sup>3</sup>*University of Vienna, Faculty of Physics and Center for Computational Materials Science, Vienna, Austria*

<sup>4</sup>*Department of Physics and Astronomy "Augusto Righi",*

*Alma Mater Studiorum - Università di Bologna, Bologna, 40127 Italy*

(Dated: February 27, 2024)

## I. FIRST PRINCIPLES METHODS

In the following, we first describe our electronic structure calculations for paramagnetic BMRO. We then proceed with the description of how the intersite exchange interaction (IEI) and Jahn-Teller (JT) terms of the full effective Hamiltonian (5) are calculated on the basis of this electronic structure. Lastly, we describe the intersite elastic coupling (EC) calculations by the Density Functional Perturbation Theory (DFPT) approach.

### A. Correlated electronic structure calculations

The electronic structure of Ba<sub>2</sub>MgReO<sub>6</sub> in the paramagnetic phase is computed with the DFT+dynamical mean-field theory(DMFT) method. The quantum impurity problem for the  $t_{2g}$  shell of the Re ion is solved within the quasi-atomic Hubbard-I (HI) approximation<sup>?</sup>; the method is abbreviated below as DFT+HI. We employ a full charge self-consistent DFT+DMFT implementation<sup>???</sup> based on the full-potential LAPW code Wien2k<sup>?</sup> that includes the spin-orbit coupling effect with the standard variational treatment.

The Wannier orbitals representing Re  $t_{2g}$  orbitals are constructed from the manifold of  $t_{2g}$  Kohn-Sham (KS) bands enclosed by the energy window [-1.36:2.04] eV relative to the KS Fermi level. The Kanamori rotationally-invariant on-site Coulomb repulsion between Re  $t_{2g}$  is parameterized by  $U_K = 3.77$  eV and  $J_H^K = 0.39$  eV, which correspond to the full  $d$ -shell parameters  $F^0 = U = 3.2$  eV and  $J_H = 0.5$  eV. Those values of  $U$  and  $J_H$  are in agreement with our previous works on  $d^1$  and  $d^2$  DP<sup>??</sup>.

The calculations of Figure 1 in the main are carried out for the experimental cubic lattice structures of Ba<sub>2</sub>MgReO<sub>6</sub> with lattice parameter  $a = 8.0802$  Å. The local density approximation of the DFT exchange-correlation potential is employed, together with 400  $\mathbf{k}$ -point mesh in the full Brillouin zone, and the Wien2k basis cutoff  $R_{\text{mt}}K_{\text{max}} = 7$ . The double-counting correction is evaluated using the fully-localized limit with the nominal  $5d$  shell occupancy of 1.

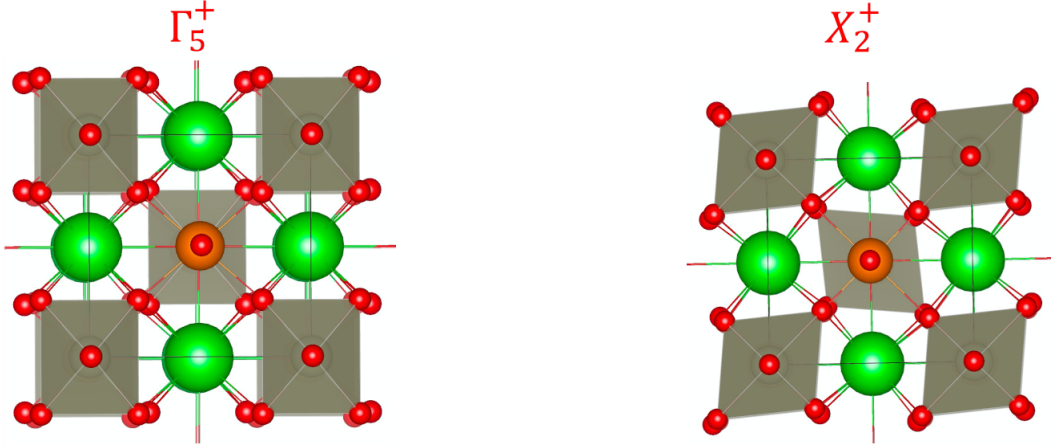
### B. Calculation $H_{IEI}$

We evaluate the IEI from the converged electronic paramagnetic electronic structure of BMRO using the force-theorem in Hubbard-I (FT-HI) approach<sup>?</sup>. This method considers small symmetry-breaking fluctuations in the density matrix of the ground state (GS)  $J_{\text{eff}} = 3/2$  multiplet that occur simultaneously on two neighboring magnetic (Re) sites  $i$  and  $j$ . The IEI  $V_{KK'}^{QQ'}(ij)$  is then evaluated by considering the response of DFT+DMFT grand potential to these two-site fluctuations. The method is similar in spirit to the force-theorem methods for the symmetry-broken magnetic state of Refs. <sup>??</sup>, but is formulated, instead, for the symmetry-unbroken paramagnetic state. The application of FT-HI in the case of BMRO is fully analogous to its previous applications to  $J_{\text{eff}} = 3/2$  DP<sup>??</sup>. The reader can thus find more detailed description in Appendix of Ref. <sup>?</sup> and Supplemenatary of Ref. <sup>?</sup>; the full derivation of the method is given in Ref. <sup>?</sup>.

### C. Calculation $H_{JT}$

Since the distortions of ReO<sub>6</sub> octahedra couple to quadrupoles and we are interested in the competition between the  $Fxy$  and  $AFx^2 - y^2$  quadrupolar orders, we consider the corresponding oxygen sublattice distortions belonging to the Brillouin zone  $\Gamma$  and  $X$ -points irreducible representations that induce  $T_{2g}$  and  $E_g$  local distortions of the

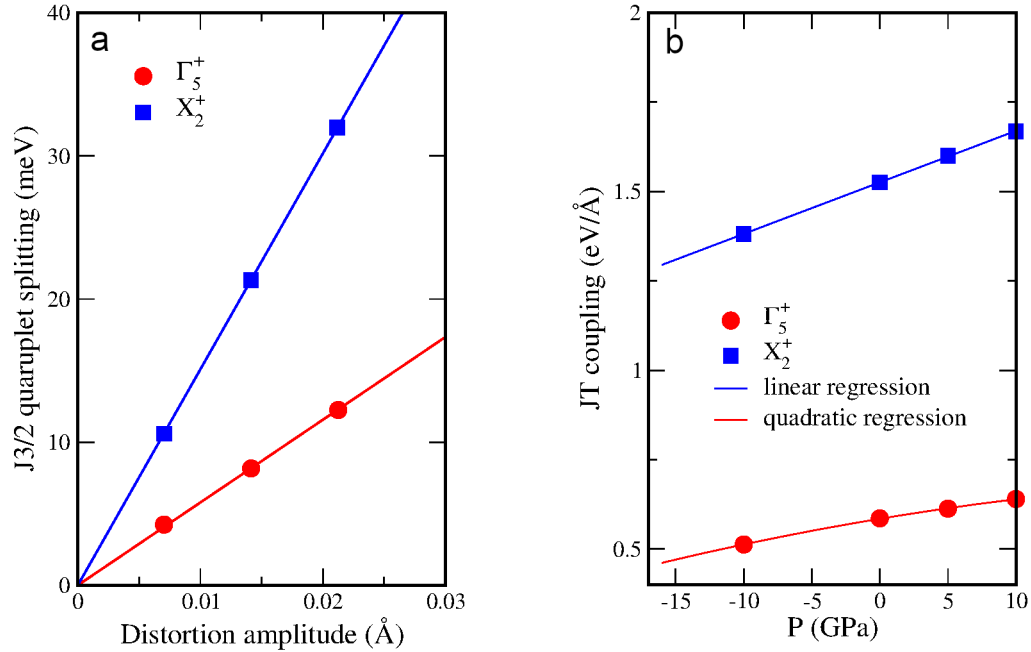
$\text{ReO}_6$  octahedra. The corresponding  $\Gamma_5^+$  and  $X_2^+$  structures (see Suppl. Fig. 1) were generated with the help of ISODISTORT tool<sup>?</sup> for a set of small distortions with the amplitude in the range from about 0.01 Å to 0.03 Å.



Supplementary Figure 1: Distorted unit cells of BMRO implementing the  $\Gamma_5^+$  and  $X_2^+$  distortions. The displayed distortion amplitude is strongly exaggerated for better visibility as compared to the distortions amplitude actually used in calculations. The plots are generated by VESTA<sup>?</sup>.

Subsequently we carry out DFT+HI calculations using the same setup as described in Sec. IA. In these self-consistent calculations, we follow the approach of Ref. ? by averaging the Boltzmann weights within the  $J_{\text{eff}}=3/2$  quadruplet in order to suppress the unphysical self-interaction contribution<sup>?</sup> to the quadruplet's splitting.

Due to the JT coupling  $-g_{\Gamma} O_2^Q q_{\Gamma Q}$ , octahedral distortions split the  $J_{\text{eff}}=3/2$  quadruplet into two Kramers doublets. The eigenvalues of normalized  $J_{\text{eff}}=3/2$  quadrupolar operators  $O_2^Q$  are  $\pm 1/2$ . Hence, the JT splitting of the quadruplet is simply given by  $g_{\Gamma} q_{\Gamma Q}$ . As shown in Suppl. Fig. 2a, the calculated splitting indeed shows a perfect linear scaling vs. the distortion amplitude  $q_{\Gamma Q}$  within the studied range, hence, no quadratic JT coupling<sup>?</sup> needs to be introduced. The larger slope in the case of  $X_2^+$  distortion is due to a stronger JT coupling to the  $E_g$  octahedral distortions.



Supplementary Figure 2: a. Calculated  $J_{\text{eff}}=3/2$  quadruplet splitting vs. distortion amplitude for BMRO at ambient pressure is shown by symbols. The lines are linear fits to the data. b. Calculated JT coupling vs. pressure (symbols). The lines are linear (for  $X_2^+$ ) and quadratic (for  $\Gamma_5^+$ ) regression fits to the data.

We repeated the same calculations for a set of volumes corresponding to compressed and expanded BMRO. The resulting JT coupling are depicted in Suppl. Fig. 2b vs. pressure (calculated from volume using our theoretical equation of states, see Sec. III); the JT coupling shows a smooth increase vs. pressure allowing to fit it with a simple linear or quadratic regression. As one sees, the  $E_g$  JT coupling is almost 3 times stronger than the  $T_{2g}$  one. Our values for the JT coupling calculated by DFT+HI agree well with the DFT results of Ref. ? .

#### D. Calculation $H_{EC}$

To determine the effective Hamiltonian  $H_{EC}$ , we utilize the projective phonon approach explained in detail in the subsequent section. For the phonon calculations in  $\text{Ba}_2\text{MgReO}_6$  we adopted the DFPT approach as incorporated in the Vienna Ab initio Simulation Package (VASP)<sup>27</sup>. These calculations involve the use of DFT with LDA exchange-correlation potential, employing a  $2 \times 2 \times 2$  k-mesh and a high energy cutoff of 600 eV together with a total energy convergence of  $10^{-6}$  eV. The choice of an LDA potential has been based on difficulties in converging accurate phonons within the Perdew-Burke-Ernzerhof exchange correlation functional. We note, however, that using LDA in this context has proven to be accurate in determining both volumetric, bond-length and pressure properties (See Suppl. Table IV and Table V). The calculations are based on a  $2 \times 2 \times 2$  supercell structure containing 32 f.u. This supercell was generated through the phonopy package<sup>28</sup> starting from a fully relaxed structure with lattice parameter of 7.9992 Å.

For the structural relaxation of the smaller 8 f.u. supercell we used the LDA potential together with a  $12 \times 12 \times 12$  k-mesh, an energy cutoff of 500 eV, and a convergence criterion of  $10^{-5}$  eV on the electronic self-consistent cycle. The volume minimization and atomic positions were optimized using a quasi-Newton algorithm with a step width of 0.2 Å and a convergence of ionic relaxation of  $10^{-3}$  eV. Detailed information about the optimized structure is available in the cif file, which is included at the conclusion of the Supplementary Material.

## II. PROJECTIVE PHONON FORMALISM

The convention used in phonopy for the dynamical matrix calculation is the following:

$$D_{\alpha\beta}(ij, \mathbf{q}) = \frac{1}{\sqrt{m_i m_j}} \sum_l \Phi_{\alpha\beta}(i0, jl) \exp(i\mathbf{q} \cdot [\mathbf{r}(jl) - \mathbf{r}(i0)]) , \quad (1)$$

where

$$\Phi_{\alpha\beta}(i0, jl) = \frac{\partial^2 V}{\partial r_{\alpha 0}(i) \partial r_{\beta l}(j)} \quad (2)$$

is the corresponding force constant matrix. Here  $(\alpha, \beta)$  represent the Cartesian coordinates,  $(i, j)$  the atomic sites and  $(0, l)$  the unit-cell index. From here on, for simplicity, we will drop the unit-cell indexes. In order to project onto the ligand ion components with specific irreducible representation coordinates, i.e.  $\Phi_{\alpha\beta}(ij) \rightarrow \Phi_{\Gamma\Gamma'}^{QQ'}(ij)$  we apply a projection operator  $C_{\Gamma Q}^\alpha$  such that  $r_{\Gamma Q} = \sum_\alpha C_{\Gamma Q}^\alpha r_\alpha$ .

$$\Phi_{\Gamma\Gamma'}^{QQ'}(ij) = \frac{\partial^2 V}{\partial r_{\Gamma Q}(i) \partial r_{\Gamma' Q'}(j)} = \sum_{\alpha, \beta} (C_{\Gamma Q}^\alpha)^t \Phi_{\alpha\beta}(ij) (C_{\Gamma' Q'}^\beta) . \quad (3)$$

Here  $\Gamma \in \{T_{2g}; E_g\}$  while  $Q$  runs over the corresponding distortions  $\{xy, xz, yz; z^2 x^2 - y^2\}$ . The Jahn-Teller irreducible representations are constituted from linear combinations of the Cartesian displacements  $X_i$ ,  $Y_i$ , and  $Z_i$  of the ligand ions situated at the vertices of the distorted octahedron. These displacements are measured relative to their positions in an undistorted reference structure, indicated by  $x_i^{(0)}, y_i^{(0)}, z_i^{(0)}$ . Employing  $X_i$ ,  $Y_i$ , and  $Z_i$ , one can construct JT normal coordinates  $Q_i$ , which adhere to the irreducible representations of the octahedral symmetry group  $O_h$ .

|          |          |   |
|----------|----------|---|
| $A_{1g}$ | $Q_1$    | $(X_2 - X_5 + Y_3 - Y_6 + Z_1 - Z_4)/\sqrt{6}$    |
| $E_g$    | $Q_2$    | $(X_2 - X_5 - Y_3 + Y_6)/2$                       |
|          | $Q_3$    | $(2Z_1 - 2Z_4 - X_2 + X_5 - Y_3 + Y_6)/2\sqrt{3}$ |
| $T_{2g}$ | $Q_{yz}$ | $(Z_3 - Z_6 + Y_1 - Y_4)/2$                       |
|          | $Q_{xz}$ | $(X_1 - X_4 + Z_2 - Z_5)/2$                       |
|          | $Q_{xy}$ | $(Y_2 - Y_5 + X_3 - X_6)/2$                       |

Supplementary Table I: The octahedral JT coordinates  $Q_i$  are defined based on the Cartesian distortions  $X_i$ ,  $Y_i$ , and  $Z_i$  of the system.

We test the consistency of the method in two cases:

1. By comparing the  $\Gamma$ -point projected frequencies against the experimental and computed ones of a non-magnetic double perovskite containing Re, i.e.  $\text{Ba}_2\text{WReO}_6$ .
2. By comparing the projected-phonon spectra to the fully computed one for  $\text{Ba}_2\text{MgReO}_6$ .

The implementation of the projective phonon formalism for calculation of EC is available on GitHub at the following link <https://github.com/dariofiosca/ElastiCouplings.git>



### A. Comparison with Ba<sub>2</sub>WReO<sub>6</sub>

We start by addressing point (1). Ba<sub>2</sub>WReO<sub>6</sub> is a non-magnetic double perovskite whose  $\Gamma$ -point irreducible phonon frequencies were determined experimentally through Raman spectroscopy<sup>?</sup> and via theoretical first-principles involving both DFT and lattice dynamic calculations (LDC)<sup>?</sup>. The  $\Gamma$ -point frequencies can be directly derived from equation 1 where  $D_{\Gamma\Gamma'}^{QQ'}(0) = 1/\sqrt{m_1 m_j} \sum_l \Phi_{\Gamma\Gamma'}^{QQ'}(0, l)$ , and their comparison is detailed in Suppl. Table III.

The phonon spectra alongside on-site and EC were calculated subsequent to a thorough DFT-based relaxation of the volume and internal atomic coordinates, using the LDA potential. For the relaxation process, a  $10 \times 10 \times 10$  k-mesh was utilized, a 400 eV cutoff for the plane wave basis, and an electronic self-consistent cycle convergence of  $10^{-4}$  eV. The final lattice parameters are listed in Table III.

For phonon calculations, a  $2 \times 2 \times 2$  supercell was constructed using the phonopy tool, and the DFPT routine in VASP was employed. The calculations were performed with an enhanced energy convergence of  $10^{-6}$  eV and an increased energy cutoff of 600 eV. Calculations included both on-site, nearest-neighbor EC, and next-nearest-neighbor EC.

Supplementary Table II: Comparison between lattice constants for Ba<sub>2</sub>WReO<sub>6</sub>. The † is used to mark the result of this work.

|         | DFT †  | Exp. 100 K <sup>?</sup> | Exp. 300 K <sup>?</sup> |
|---------|--------|-------------------------|-------------------------|
| $a$ (Å) | 8.1046 | 8.1010                  | 8.1120                  |

Supplementary Table III: The first column represents the computed irreducible frequencies as  $\Gamma$  obtained from phonopy, while the second are the ones obtained from the projective method including onsite JT and both nearest and next nearest neighbors EC. The † represents the results of this work. The third column includes the experimentally defined Raman modes at 300 K and the comparison with experimental data at 300 K on the ceramic material, together with two theoretical calculations of phonon spectra.

| R. mod.  | Phonopy† | Projected† | Exp. Ref. <sup>?</sup> | Exp Ref. <sup>?</sup> | DFT Ref. <sup>?</sup> | LDC Ref. <sup>?</sup> |
|----------|----------|------------|------------------------|-----------------------|-----------------------|-----------------------|
| $E_g$    | 534      | 492        | 536                    | 538                   | 614                   | 522                   |
| $T_{2g}$ | 421      | 418        | 439                    | 441                   | 405                   | 432                   |
| $A_{1g}$ | 780      | 784        | 807                    | 812                   | 833                   | 776                   |

### B. Comparison phonons in BMRO

From the projected force constant matrix  $\Phi_{\Gamma\Gamma'}^{QQ'}(ij)$  it is possible to recalculate the Dynamical Matrix

$$D_{\Gamma\Gamma'}^{QQ'}(\mathbf{q}) = \frac{1}{\sqrt{m_Q m_{Q'}}} \sum_{ij} \Phi_{\Gamma\Gamma'}^{QQ'}(ij) \exp(i\mathbf{q} \cdot [\mathbf{r}_\Gamma^Q(i) - \mathbf{r}_{\Gamma'}^{Q'}(j)]) \quad (4)$$

where  $(m_Q, m_{Q'})$  are the oxygen masses, and  $\mathbf{q}$  the wave vector. The equation of motion can be derived to be

$$\sum_{\Gamma'\gamma'} D_{\Gamma\Gamma'}^{QQ'}(\mathbf{q}) e_{\Gamma'}^{Q'}(\mathbf{q}\nu) = [\omega(\mathbf{q}\nu)]^2 e_\Gamma^Q(\mathbf{q}\nu) \quad (5)$$

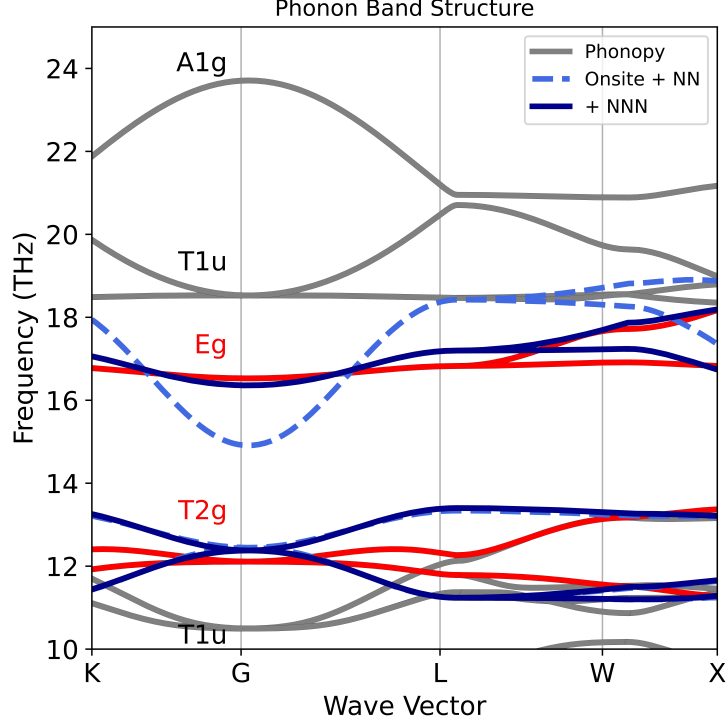
and via diagonalization of the equation of motion one obtains the phonon spectra.

This methodology serves to evaluate the precision of the projective phonon technique in comparison to the full phonon calculation of the 32 f.u. supercell. It's important to highlight that the inclusion of next-nearest neighbors (NNN) EC is crucial for achieving a high degree of accuracy in the phonon band structure at the  $\Gamma$  and  $X$  points.

While incorporating ECs beyond NNN can refine the phonon spectra comparison, this does not necessarily yield a physically comprehensive solution, as the octahedra beyond NNN are impacted by the supercell's periodic boundary conditions.

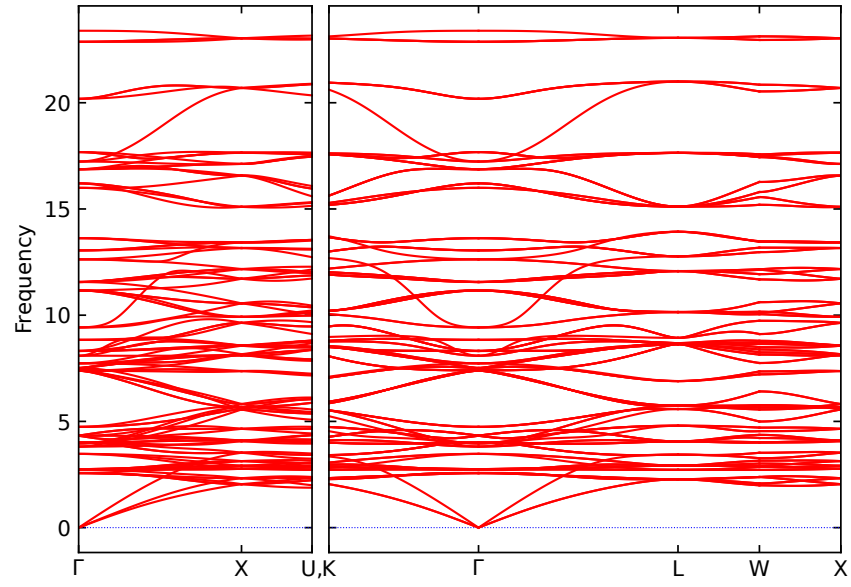
We note that the current has its main limitation in the DFPT implementation of VASP, which only calculates the force constant at the  $\Gamma$ -point. An accurate computation of the force constants at other  $\mathbf{q}$  points requires the use

of significantly larger supercell structures. However, scaling up the supercell size poses substantial computational challenges. Fortunately, for BMRO extensive supercell calculations are not mandatory. As demonstrated in Suppl. Fig. 3, we achieve satisfactory convergence at the  $\Gamma$  and  $X$  high-symmetry points by incorporating on-site, nearest-neighbor (NN), and NNN intersite elastic couplings.

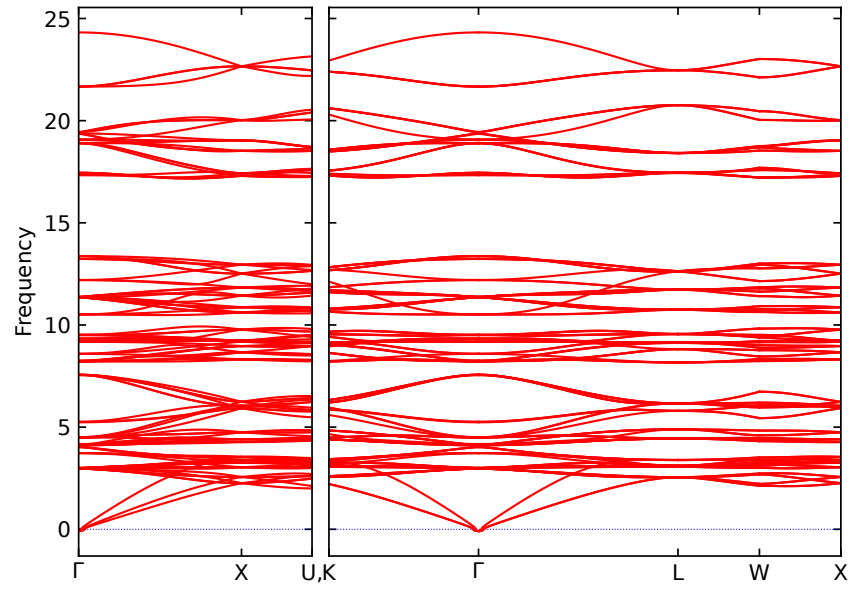


Supplementary Figure 3: Comparison between primitive cell phonons of  $\text{Ba}_2\text{MgReO}_6$  computed with phonopy and the reconstructed phonons reconstructed from the projected force constant matrix  $\Phi_{\Gamma\Gamma'}^{QQ'}(ij)$ . The red lines mark the  $E_g$  and  $T_{2g}$  phononic bands, while the dotted light blue are the reconstructed bands from onsite + NN EC and the solid blue line mark the reconstructed bands from onsite + NN + NNN.

### C. Phonon Band-structures $\text{Ba}_2\text{WReO}_6$ and $\text{Ba}_2\text{MgReO}_6$



Supplementary Figure 4: Phonon bandstructure of  $\text{Ba}_2\text{WReO}_6$ . Frequencies are in THz.



Supplementary Figure 5: Phonon bandstructure of  $\text{Ba}_2\text{MgReO}_6$ . Frequencies are in THz.

### III. EQUATION OF STATE

To compute the volumes at different pressure we fit the pressure as function of volume with the Birch-Murnaghan Equation of State (EOS)

$$P = \frac{3}{2}B_0 \left[ \left( \frac{V}{V_0} \right)^{-7/3} - \left( \frac{V}{V_0} \right)^{-5/3} \right] \times \left\{ 1 + \frac{3}{4}(B'_0 - 4) \left[ \left( \frac{V}{V_0} \right)^{-2/3} - 1 \right] \right\} \quad (6)$$

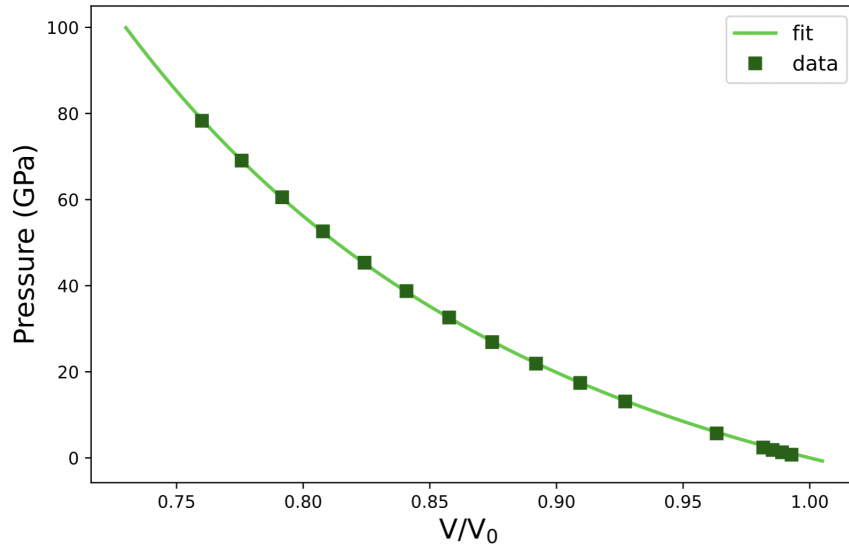
The volumetric calculations were done in DFT by employing the VASP package with the 8 f.u. cubic supercell, starting from the fully relaxed solution described in Section ID. The LDA potential is used, together with a k-mesh of  $12 \times 12 \times 12$  and energy cutoff of 600 eV with energy convergence of the self consistent cycle of  $10^{-5}$  eV. The results in Table IV have been compared with both experimental and first-principles calculation from Ref. and Ref.<sup>?</sup> respectively.

Supplementary Table IV: Calculated bulk modulus ( $B_0$  in GPa) and derivative of bulk modulus ( $B'_0$ ).

|             | DFT (this work) | DFT <sup>?</sup> |
|-------------|-----------------|------------------|
| $B_0$ (GPa) | 197.47          | 158.27           |
| $B'_0$      | 4.51            | 4.80             |

Supplementary Table V: Calculated lattice constant and bondlength distances.

|          | DFT (this work) | Exp. Ref <sup>?</sup> | DFT <sup>?</sup> |
|----------|-----------------|-----------------------|------------------|
| $a$ (Å)  | 7.99292         | 8.0802                | 8.1790           |
| Re-O (Å) | 1.92            | 1.96                  | 1.95             |
| Mg-O (Å) | 2.08            | 2.08                  | 2.14             |
| Ba-O (Å) | 2.83            | 2.85                  | 2.89             |



Supplementary Figure 6: Fit of Pressure vs volumetric DFT solution with Birch-Murnaghan EOS.

From the EOS we derived for both the Experimental and DFT-relaxed structures, the evolution of the lattice constant with pressure. In the following table we report the values used to calculate  $H_{IEI}$  and  $H_{IEC}$ .

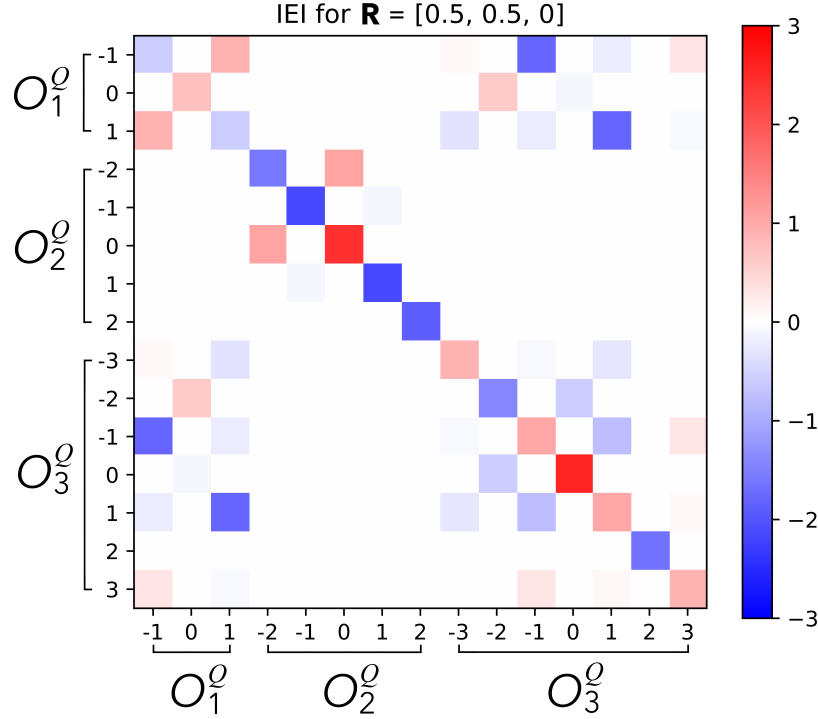
Supplementary Table VI: Calculated lattice constant from  $\text{Ba}_2\text{MgReO}_6$  EOS employed for the calculation of IEI and EC.

| Pressure (GPa) | IEI $a$ (Å) | IEC $a$ (Å) |
|----------------|-------------|-------------|
| -10            | 8.3058      | 8.22258     |
| -5             | 8.1810      | 8.09898     |
| 0              | 8.0802      | 7.99292     |
| 5              | 7.9954      | 7.91524     |
| 10             | 7.9221      | 7.84270     |

#### IV. INTERSITE EXCHANGE INTERACTIONS

In Suppl. Fig. 7 we plot the IEI in BMRO at zero pressure as a color map; the IEI values are also listed in Suppl. Table VII for several values of pressure. One sees that the quadrupole IEI block includes, apart from antiferroic  $e_g$  coupling, also ferroic  $t_{2g}$  ones. These  $t_{2g}$  ferroic IEI have not been previously included in model electronic effective Hamiltonians of  $d^1$  DP<sup>???</sup>. The  $t_{2g}$  IEI are the reason why the  $Fxy$  quadrupole order dominates over the  $\text{AF}x^2-y^2$  one when the EL coupling is neglected.

One may also notice significant octupolar IEI, which are the largest couplings among time-odd IEI.



Supplementary Figure 7: Color map of the IEI  $V_{KK'}^{QQ'}$  in BMRO at pressure 0 GPa for the  $[1/2, 1/2, 0]$  Re-Re pair. All values are in meV. The numerical list of  $V_{KK'}^{QQ'}$  is given in Suppl. Table VII.

Supplementary Table VII: Calculated IEI  $V_{KK'}^{QQ'}$  for the  $J_{eff}=3/2$  multiplet. First two columns list  $Q$  and  $Q'$ , respectively. Third and fourth column displays the  $KQ$  and  $K'Q'$  tensors in the Cartesian representation, respectively. The last three columns displays the values of IEI (in meV) for the  $[1/2,1/2,0]$  nearest-neighbor Re-Re bond in  $\text{Ba}_2\text{MgReO}_6$  for pressure 10 GPa, ambient condition and -16 GPa, respectively.

| Pressure              |    |               |               | 10 GPa | Ambient | -16 GPa<br>( $\text{Ba}_2\text{CaReO}_6$ volume) |
|-----------------------|----|---------------|---------------|--------|---------|--|
| Dipole-Dipole         |    |               |               |        |         |  |
| -1                    | -1 | y             | y             | -0.79  | -0.59   | -0.31  |
| 0                     | 0  | z             | z             | 1.00   | 0.73    | 0.38   |
| 1                     | -1 | x             | y             | 0.99   | 0.91    | 0.73   |
| 1                     | 1  | x             | x             | -0.79  | -0.59   | -0.31  |
| Quadrupole-Quadrupole |    |               |               |        |         |  |
| -2                    | -2 | xy            | xy            | -2.07  | -1.59   | -0.94  |
| -1                    | -1 | yz            | yz            | -2.67  | -2.14   | -1.38  |
| 0                     | -2 | $z^2$         | xy            | 1.19   | 1.08    | 0.84   |
| 0                     | 0  | $z^2$         | $z^2$         | 3.05   | 2.43    | 1.55   |
| 1                     | -1 | xz            | yz            | -0.10  | -0.10   | -0.08  |
| 1                     | 1  | xz            | xz            | -2.67  | -2.14   | -1.38  |
| 2                     | 2  | $x^2-y^2$     | $x^2-y^2$     | -2.36  | -1.89   | -1.23  |
| Octupole-Octupole     |    |               |               |        |         |  |
| -3                    | -3 | $y(x^2-3y^2)$ | $y(x^2-3y^2)$ | 1.16   | 0.88    | 0.50   |
| -2                    | -2 | xyz           | xyz           | -1.85  | -1.42   | -0.84  |
| -1                    | -3 | $yz^2$        | $y(x^2-3y^2)$ | -0.08  | -0.09   | -0.08  |
| -1                    | -1 | $yz^2$        | $yz^2$        | 1.23   | 1.03    | 0.75   |
| 0                     | -2 | $z^3$         | xyz           | -0.64  | -0.60   | -0.49  |
| 0                     | 0  | $z^3$         | $z^3$         | 3.13   | 2.56    | 1.75   |
| 1                     | -3 | $xz^2$        | $y(x^2-3y^2)$ | -0.32  | -0.28   | -0.21  |
| 1                     | -1 | $xz^2$        | $yz^2$        | -0.83  | -0.76   | -0.61  |
| 1                     | 1  | $xz^2$        | $xz^2$        | 1.23   | 1.03    | 0.75   |
| 2                     | 2  | $z(x^2-y^2)$  | $z(x^2-y^2)$  | -2.06  | -1.65   | -1.06  |
| 3                     | -1 | $x(3x^2-y^2)$ | $yz^2$        | 0.32   | 0.28    | 0.21   |
| 3                     | 1  | $x(3x^2-y^2)$ | $xz^2$        | 0.08   | 0.09    | 0.08   |
| 3                     | 3  | $x(3x^2-y^2)$ | $x(3x^2-y^2)$ | 1.16   | 0.88    | 0.50   |
| Dipole-Octupole       |    |               |               |        |         |  |
| -1                    | -3 | y             | $y(x^2-3y^2)$ | 0.07   | 0.08    | 0.07   |
| -1                    | -1 | y             | $yz^2$        | -2.25  | -1.79   | -1.15  |
| -1                    | 1  | y             | $xz^2$        | -0.23  | -0.21   | -0.17  |
| -1                    | 3  | y             | $x(3x^2-y^2)$ | 0.36   | 0.31    | 0.23   |
| 0                     | -2 | z             | xyz           | 0.69   | 0.61    | 0.47   |
| 0                     | 0  | z             | $z^3$         | -0.15  | -0.12   | -0.09  |
| 1                     | -3 | x             | $y(x^2-3y^2)$ | -0.36  | -0.31   | -0.23  |
| 1                     | -1 | x             | $yz^2$        | -0.23  | -0.21   | -0.17  |
| 1                     | 1  | x             | $xz^2$        | -2.25  | -1.79   | -1.15  |
| 1                     | 3  | x             | $x(3x^2-y^2)$ | -0.07  | -0.08   | -0.07  |



## V. INTERSITE ELASTIC COUPLINGS

Supplementary Table VIII: The Table displays the calculated values of EC  $\Phi_{\Gamma\Gamma'}^{QQ'}(ij)$  for  $(ij)$  being the on-site  $(ii)$  component, the irreducible ligand components  $(ij)$  connecting NN Re-Re octahedral centers with  $\mathbf{R} = [1/2, 1/2, 0]$  and the irreducible ligand components  $(ij)$  connecting NNN Re-Re centers with  $\mathbf{R} = [1, 0, 0]$ . First two columns list  $Q$  and  $Q'$ , respectively. Units are in eV/Å<sup>2</sup>.

| On site elastic couplings                               |        |        |        |        |        |
|---|--------|--------|--------|--------|--------|
|   | xy     | yz     | z2     | xz     | x2-y2  |
|   | 9.633  | 9.633  | 21.822 | 9.633  | 21.822 |
| Nearest-Neighbors EC for $\mathbf{R} = [0.5, 0.5, 0]$   |        |        |        |        |        |
|   | xy     | yz     | z2     | xz     | x2-y2  |
| xy  | 0.584  | 0      | -0.463 | 0      | 0      |
| yz  | 0      | -0.229 | 0      | -0.250 | 0      |
| z2  | -0.463 | 0      | 0.532  | 0      | 0      |
| xz  | 0      | -0.250 | 0      | -0.229 | 0      |
| x2-y2   | 0      | 0      | 0      | 0      | -1.745 |
| Next-Nearest-Neighbors IEC for $\mathbf{R} = [1, 0, 0]$ |        |        |        |        |        |
|   | xy     | yz     | z2     | xz     | x2-y2  |
| xy  | -0.041 | 0      | 0      | 0      | 0      |
| yz  | 0      | 0.027  | 0      | 0      | 0      |
| z2  | 0      | 0      | 0.446  | 0      | -0.082 |
| xz  | 0      | 0      | 0      | -0.041 | 0      |
| x2-y2   | 0      | 0      | -0.082 | 0      | 0.541  |

## VI. MEAN-FIELD APPROACH TO THE IEI+EL EFFECTIVE HAMILTONIAN

We solve the full many-body effective Hamiltonian (eq. 1 of the main text) using a generalized single-site mean-field theory. Both the IEI (eq. 2 of the main text) and EC (eq. 4 *ibid*) intersite terms are mean-field decoupled; the resulting single-site JT problem in electronic and elastic mean fields is treated fully quantum-mechanically. This mean-field approach to the cooperative JT effect is described in a number of references<sup>???</sup>; here we implement it for the most general linear JT coupling and mean-field potential within the  $J_{\text{eff}}=3/2$  space. For consistency, we outline the derivation of this mean-field scheme and fully specify the solution of the single-site JT problem below.

We label the sites in a given ordered phase by the translational vector  $\mathbf{l}$  labeling magnetic unit cells and the basis (sublattice) vector  $\boldsymbol{\tau}$  within the magnetic unit cell. The intersublattice IEI and EC are

$$V_{KK'}^{QQ'}(\boldsymbol{\tau}\boldsymbol{\tau}') = \sum_{\langle ij \rangle} \sum_{\mathbf{l}} V_{KK'}^{QQ'}(ij) \delta(\mathbf{R}_{ij} - \mathbf{l} - \boldsymbol{\tau}' + \boldsymbol{\tau})$$

and

$$\Phi_{\Gamma\Gamma'}^{QQ'}(\boldsymbol{\tau}\boldsymbol{\tau}') = \sum_{\langle ij \rangle} \sum_{\mathbf{l}} \Phi_{\Gamma\Gamma'}^{QQ'}(ij) \delta(\mathbf{R}_{ij} - \mathbf{l} - \boldsymbol{\tau}' + \boldsymbol{\tau}),$$

respectively.

The mean-field decoupling of the IEI and EC terms then reads

$$H_{\text{IEI}}^{\text{MF}} = \sum_{\boldsymbol{\tau}KQ} \left( O_K^Q(\boldsymbol{\tau}) - \frac{1}{2} \langle O_K^Q(\boldsymbol{\tau}) \rangle \right) V_{KQ}^{\text{MF}}(\boldsymbol{\tau}), \quad (7)$$

$$H_{\text{EC}}^{\text{MF}} = \sum_{\tau \Gamma} \sum_{Q \in \Gamma} \left( q_{\Gamma Q}(\tau) - \frac{1}{2} \langle q_{\Gamma Q}(\tau) \rangle \right) \Phi_{\Gamma Q}^{\text{MF}}(\tau), \quad (8)$$

where the respective IEI and EC mean fields are

$$V_{KQ}^{\text{MF}}(\tau) = \sum_{K'Q'\tau'} V_{KK'}^{QQ'}(\tau\tau') \langle O_{K'}^{Q'}(\tau') \rangle$$

and

$$\Phi_{\Gamma Q}^{\text{MF}}(\tau) = \sum_{\Gamma'\tau'} \sum_{Q' \in \Gamma'} \Phi_{\Gamma\Gamma'}^{QQ'}(\tau\tau') \langle q_{\Gamma'Q'}(\tau') \rangle.$$

The single-site JT problem in mean-field at a given site  $\tau$  is then given by the single-site Hamiltonian (eq. 3 of the main text) plus the mean-field terms:

$$H_{1s} = \sum_{\Gamma} \sum_{Q \in \Gamma} \left[ \frac{p_Q^2}{2M_{\Gamma}} + \Phi_{\Gamma} \frac{q_{\Gamma Q}^2}{2} - g_{\Gamma} O_2^Q q_{\Gamma Q} \right] + H_{\text{IEI}}^{\text{MF}} + H_{\text{EC}}^{\text{MF}}, \quad (9)$$

where from now on we omit the  $\tau$  label for brevity.

We diagonalize the harmonic oscillator terms in (9) and quantize accordingly the displacements  $q_{\Gamma Q}$  in the JT and EC terms. Omitting the constant  $-\frac{1}{2} \langle \dots \rangle$  terms in (7) and (8), the resulting Hamiltonian for the single-site JT problem reads

$$H_{1s} = \sum_{\Gamma} \sum_{Q \in \Gamma} \left[ \hbar\omega_{\Gamma}(\hat{n}_{\Gamma Q} + 1/2) + (\Phi_{\Gamma}^{\text{MF}} - g_{\Gamma} O_2^Q) A_{\Gamma}(a_{\Gamma Q}^{\dagger} + a_{\Gamma Q}) \right] + \sum_{KQ} V_{KQ}^{\text{MF}} O_K^Q, \quad (10)$$

where we introduced creation(annihilation) operators  $a_{\Gamma Q}^{\dagger}(a_{\Gamma Q})$  for the local octahedral vibration mode  $\Gamma Q$ ,  $\hat{n}_{\Gamma Q} = a_{\Gamma Q}^{\dagger} a_{\Gamma Q}$ . The oscillator strength  $\hbar\omega_{\Gamma}$ , where  $\omega_{\Gamma} = \sqrt{\Phi_{\Gamma}/M_{\Gamma}}$ , calculated with ab initio on-site elastic couplings  $\Phi_{\Gamma}$  (Table VIII) is equal to 75.3 (49.8) meV for the  $E_g$  ( $T_{2g}$ ) modes, respectively. The quantized displacements  $A_{\Gamma}(a_{\Gamma Q}^{\dagger} + a_{\Gamma Q}) = q_{\Gamma Q}$ , where  $A_{\Gamma} = \sqrt{\hbar/(2M_{\Gamma}\omega_{\Gamma})}$  is equal to 4.17(5.12) pm for the  $E_g$ ( $T_{2g}$ ) modes.

In order to solve the Hamiltonian (10) we introduce a normalized mixed (vibronic) basis  $|\phi_i\rangle = |M_i\rangle \times |\mathbf{n}_i\rangle$ , where  $\langle \phi_i | \phi_j \rangle = \delta_{ij}$ , the electronic state  $|M\rangle \equiv |J_{\text{eff}}; M\rangle$  is the eigenstate of  $\hat{J}_{\text{eff}}$  with the projection  $M$ ,  $|\mathbf{n}\rangle \equiv |n_{E_g z^2}, n_{E_g x^2-y^2}, n_{T_{2g} xy}, n_{T_{2g} xz}, n_{T_{2g} yz}\rangle \equiv |\hat{\mathbf{n}}_{\Gamma Q}, n_{\Gamma Q}\rangle$  is the local phonon modes occupancies. For convenience, we introduce here another notation,  $\tilde{\mathbf{n}}_{\Gamma Q}$ , to designate the occupancies of all modes except the  $\Gamma Q$  one. In this basis, the matrix elements of different operators in (10) read

$$\begin{aligned} \langle \phi_i | O_K^Q | \phi_j \rangle &= \delta_{\mathbf{n}_i, \mathbf{n}_j} \left[ O_K^Q \right]_{M_i M_j}, \\ \langle \phi_i | \hbar\omega_{\Gamma}(\hat{n}_{\Gamma Q} + 1/2) | \phi_j \rangle &= \delta_{i,j} \hbar\omega_{\Gamma}(n_{\Gamma Q} + 1/2), \\ \langle \phi_i | a_{\Gamma Q}^{\dagger} + a_{\Gamma Q} | \phi_j \rangle &= \delta_{M_i, M_j} \delta_{\tilde{\mathbf{n}}_{\Gamma Q}^i, \tilde{\mathbf{n}}_{\Gamma Q}^j} \left( \delta_{n_{\Gamma Q}^i, n_{\Gamma Q}^j+1} \sqrt{n_{\Gamma Q}^i} + \delta_{n_{\Gamma Q}^i+1, n_{\Gamma Q}^j} \sqrt{n_{\Gamma Q}^j} \right). \end{aligned} \quad (11)$$

We cut the basis  $\{|\phi\rangle\}$  at a chosen maximum phonon number  $N_{\text{ph}}^{\text{MAX}} = \text{MAX} \left[ \sum_{\Gamma Q} n_{\Gamma Q} \right]$ . Once all matrix elements  $\langle \phi_i | H_{1s} | \phi_j \rangle$  have been evaluated with the help of (11), we diagonalize  $H_{1s}$  and recalculate the electronic moments  $\langle O_K^Q \rangle$ , displacements  $\langle q_{\Gamma Q} \rangle$ , total and free energy for a given site. Having solved the single-site JT problem for all sites  $\tau$  in the structure, we recalculate the exchange (7) and elastic (8) mean fields to close the mean-field cycle.

This mean-field approach is implemented in the framework of "McPhase" package<sup>7</sup> as an in-house module. As initial guesses of the mean-field procedure we employ all  $1\mathbf{k}$  structures realizable within the BMRO single conventional unit cell that contains 4 magnetic Re sites.

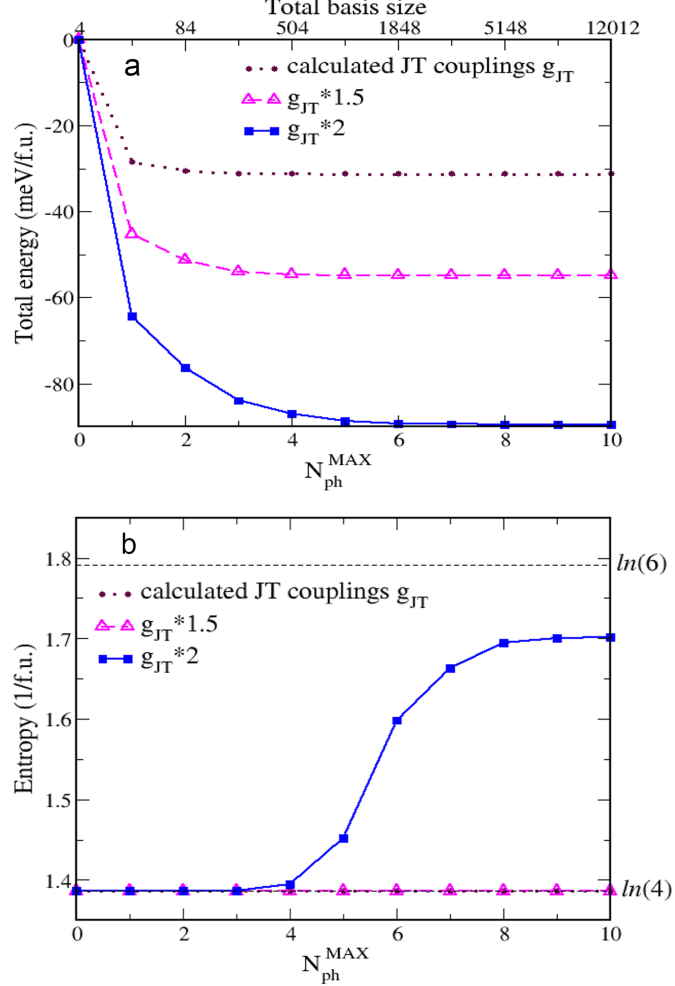
## VII. EFFECT OF THE VIBRONIC BASIS CUTOFF AND JAHN-TELLER REGIME

In order to benchmark the convergence of the numerical solution of the JT problem (10) with respect to the vibronic basis cutoff  $N_{\text{ph}}^{\text{MAX}}$ , we solved this problem, without the mean-field terms, varying  $N_{\text{ph}}^{\text{MAX}}$ . The JT problem in this

case reduces to the single-site term (eq. 3 of the main text), which in the quantized form reads

$$H_{JT} = \sum_{\Gamma} \sum_{Q \in \Gamma} \hbar \omega_{\Gamma} (\hat{n}_{\Gamma Q} + 1/2) - g_{\Gamma} O_2^Q A_{\Gamma} (a_{\Gamma Q}^{\dagger} + a_{\Gamma Q}). \quad (12)$$

We employ the values of parameters ( $g_{\Gamma}$ ,  $\omega_{\Gamma}$ , and  $A_{\Gamma}$ ) that are calculated for BMRO at ambient pressure (see the previous section and Suppl. Fig. 2b).



Supplementary Figure 8: Total energy (a) and entropy (b) of the single-site JT problem ground state as a function of the basis cutoff  $N_{\text{ph}}^{\text{MAX}}$ . The size of the corresponding basis is indicated by the upper tick labels of panel a.

In Suppl. Figs. 8a and 8b we display the calculated total energy (omitting the zero-point contribution) and entropy vs.  $N_{\text{ph}}^{\text{MAX}}$ . One sees that already for  $N_{\text{ph}}^{\text{MAX}} = 1$ , corresponding to the weak coupling treatment of the JT problem, the total energy is quite well converged, while the entropy still corresponds to the ground-state quadruplet and is not affected by including local phonons into the basis. In order to explore the limits of the weak-coupling treatment, we also ran the same calculation with the JT coupling strength artificially increased. With the JT coupling scaled by the factors 1.5 and 2, the weak-coupling treatment clearly becomes insufficient for the total energy. The ground-state degeneracy markedly increases once the JT coupling becomes twice larger, indicating that the JT ground-state solutions are now localized within the "trough" of the JT potential energy surface?

## VIII. RELAXED BMRO STRUCTURE

```

# CIF file created by FINDSYM, version 7.1.3

data_findsym-output
_audit_creation_method FINDSYM

_cell_length_a      7.9991900000
_cell_length_b      7.9991900000
_cell_length_c      7.9991900000
_cell_angle_alpha   90.0000000000
_cell_angle_beta    90.0000000000
_cell_angle_gamma   90.0000000000
_cell_volume        511.8444957459

_symmetry_space_group_name_H-M "F 4/m -3 2/m"
_symmetry_Int_Tables_number 225
_space_group.reference_setting '225:-F 4 2 3'
_space_group.transform_Pp_abc a,b,c;0,0,0

_atom_site_label
_atom_site_type_symbol
_atom_site_symmetry_multiplicity
_atom_site_Wyckoff_symbol
_atom_site_fract_x
_atom_site_fract_y
_atom_site_fract_z
_atom_site_occupancy
_atom_site_fract_symmform
Mg1 Mg   4 a  0.00000  0.00000  0.00000  1.00000  0,0,0
Re1 Re   4 b  0.50000  0.50000  0.50000  1.00000  0,0,0
Ba1 Ba   8 c  0.25000  0.25000  0.25000  1.00000  0,0,0
O1  O   24 e  0.25951  0.00000  0.00000  1.00000  Dx,0,0

# end of cif

```